


## Beam based characterization of the European Synchrotron Radiation Facility Extremely Brilliant Source short range wakefield model

L. R. Carver<sup>1</sup>,\* T. Brochard, E. Buratin<sup>1</sup>, N. Carmignani<sup>1</sup>, F. Ewald,  
L. Hoummi<sup>1</sup>, S. M. Liuzzo<sup>1</sup>, T. Perron, B. Roche<sup>1</sup>, and S. White<sup>1</sup>  
*European Synchrotron Radiation Facility, 38000 Grenoble, France*

 (Received 17 June 2022; accepted 7 April 2023; published 27 April 2023)

The European Synchrotron Radiation Facility (ESRF) storage ring (SR) has been dismantled and replaced by the Extremely Brilliant Source (EBS) which has now been commissioned. This new fourth generation light source has much smaller vacuum chambers than its predecessor, which necessitates a careful optimization of the vacuum systems and an accurate impedance model to be able to deliver all beam modes at the design current and predict future machine performance in the presence of strong collective effects. This paper will report on the first beam based measurements with a single bunch in order to characterize the short range wakefield model of the EBS SR and to make a first comparison with predictions. The results from transverse instability thresholds and tune shift measurements will be presented, as well as bunch length and phase variation with the current. Microwave instability threshold measurements have shown some discrepancy with predictions, which could arise from welding defects in the machining of the chambers. These discrepancies and other possible causes will be discussed.

DOI: [10.1103/PhysRevAccelBeams.26.044402](https://doi.org/10.1103/PhysRevAccelBeams.26.044402)

### I. INTRODUCTION

The ESRF-EBS is a new fourth generation light source, which started commissioning in 2019 and has been in user operation mode (USM) since 2020 [1,2]. The EBS lattice is based on the hybrid multibend achromat (HMBA) concept, which has reduced the horizontal emittance from around 4000 pm rad (from the previous SR which was based on a double bend achromat [DBA] lattice) to 133 pm rad [3]. The reduction in the horizontal emittance has allowed the EBS to produce light with brilliance and spatial coherence that is larger than its predecessor [4]. A comparison between the main parameters of the HMBA lattice and the old ESRF DBA lattice can be found in Table I. In achieving this low emittance, much stronger field gradients were needed than in the previous machine. These stronger fields are realized by reducing the magnet bore radius and consequently the aperture of the vacuum vessels.

There are several filling modes in routine operation at the ESRF [5]. The most frequently used is called “7/8 + 1” which consists of 7/8 of the ring being uniformly filled (with 192 mA), with 1 high current bunch (8-mA design current) in the middle of the 1/8 gap. There are also two

filling modes that are used for timing experiments on the beam lines, which are composed of symmetrically placed high current bunches with large interbunch spacing. These two filling modes are “4 × 10” which is 4 bunches of 10 mA current and “16 bunch” which is 92-mA total current distributed over 16 bunches. In the old ESRF SR, the two timing modes were challenging to operate due to the strong collective effects coming from the combination of high bunch current and a poorly optimized machine impedance. The 4 × 10 required a dedicated high chromaticity optics in order to be able to inject without triggering head-tail instabilities [6] which caused injection saturation, and the 16-bunch mode had significant power deposition and caused problems relating to the heating of equipment [7]. It was decided that all filling modes would be kept in operation for the EBS. As opposed to several ongoing upgrade projects [8,9], the ESRF-EBS baseline design did not integrate a bunch lengthening harmonic cavity that would have partially mitigated the negative impact of beam coupling impedance. This posed a risk for operation and a challenge for the vacuum chambers, which necessitated a careful design and optimization in order to be able to run with such high bunch currents with the reduced aperture from the restart of USM.

When reducing the aperture of the vacuum chambers, the beam coupling impedance is significantly increased and can cause severe limitations from beam instabilities or other collective effects when operating with high single bunch currents [10]. These limitations can then be mitigated by utilizing either a transverse feedback or running with high

\*lee.carver@esrf.fr

Published by the American Physical Society under the terms of the *Creative Commons Attribution 4.0 International* license. Further distribution of this work must maintain attribution to the author(s) and the published article's title, journal citation, and DOI.

TABLE I. Main design parameters of the ESRF-EBS storage ring.

	Units	DBA	HMBA
Energy	GeV	6.04	6
Circumference	m	844.391	843.977
Maximum total current	mA	200	200
Maximum single bunch current	mA	10	10
Maximum number of bunches		992	992
Average horizontal $\beta$	m	21.41	4.16
Average vertical $\beta$	m	23.28	7.66
Horizontal emittance	pm rad	3993	133
Momentum compaction factor	$10^{-5}$	17.795	8.512
Momentum spread (@0 mA)	$10^{-3}$	1.062	0.9356
Bunch length (@0 mA)	mm	4.67	3.06
Energy loss/turn	MeV/turn	4.879	2.533
rf voltage	MV	8.0	6.0
Synchrotron tune	$10^{-3}$	5.429	3.490

chromaticities [11]. A compromise between beam stability and other SR parameters such as injection efficiency or lifetime is often necessary to provide optimal operating conditions. To further improve its performance in the near future, the ESRF-EBS storage ring may be pushed into more challenging and complex running scenarios such as a further increased single bunch current or reduced vertical gaps in straight section chambers and in-vacuum undulators (IVU). These can increase the impedance contribution from these elements and therefore its effects on beam stability or beam-induced heating of key components and degrade the overall SR performance [12].

The development of accurate impedance models is now a high priority for many facilities that are planning to upgrade their existing machine from the third to the fourth generation. The beam based characterization that will be described in this paper has given confidence to future machine upgrades, both in the quality of the prediction of machine performance of a low aperture machine and also in the ability to test mitigation methods. The development of the ESRF-EBS short range wakefield model will be described, followed by a comparison between tracking simulations and the first collective effects measurements of the EBS. The origin of discrepancies between the model and the measurements will be discussed as they are seen.

## II. MINIMIZING THE IMPEDANCE OF THE SR

The HMBA lattice and more generally ultralow emittance lattices based on the multi bend achromat concept require strong focusing and sextupoles often leading to a reduction of the magnets and vacuum chamber aperture. In the case of the EBS, upgrading from the DBA lattice to the HMBA lattice resulted in a vertical full aperture reduction from 32 to 20 mm in medium focusing regions and 13 mm in strong focusing regions [13]. The straight sections

chambers aperture was maintained at 8 mm. Figure 1 shows the EBS 20-mm vertical gap chamber profile, a similar design is found in the strong focusing region.

In addition to this reduction of aperture that enhances impedance, the HMBA lattice features a shorter bunch length, and smaller momentum spread and momentum compaction factor, as seen in Table I. This increases the effect of impedance on the beam. The impact of these unfavorable beam parameters is nevertheless partially compensated in the transverse planes by the reduction of  $\beta$  functions.

In order to ensure the delivery of high bunch current modes, several constraints and mitigation measures were adopted at the early design stage of the ESRF-EBS ring. These are summarized as follows: (i) ensure smooth transitions by setting a limit of all taper angles to  $5^\circ$ , except for the special case of IVU and radio-frequency (rf) straight sections; (ii) enforce electrical continuity and constant chamber profile at  $\pm 25$  mm horizontally from the beam axis (except for the necessary transitions to the straight section and strong focusing apertures). This also maintains the aperture symmetry (see Fig. 1) and prevents introducing strong constant impedance contributions [14]; (iii) place all absorbers and pumping ports in the antechambers; (iv) change the material of the dipole chamber from stainless steel ( $\sigma_c = 1.45 \times 10^6$  S/m) to aluminum ( $\sigma_c = 37.7 \times 10^6$  S/m) where  $\sigma_c$  is the material conductivity. The dipole filling factor is 38%; (v) all mechanical elements directly seen by the beam have to be modeled and validated with electromagnetic (EM) simulation codes.

Some elements required special attention, either because of their large number of occurrences or their significant contribution to the overall impedance budget [15]. All optimization studies were done with CST Particle Studio [16].

In particular, there are approximately 550 flanges and 450 bellows shielded with so-called rf fingers distributed around the ring that can have a strong impact on the impedance budget if not properly optimized. Low impedance flat sealed flanges, similar to the proposal presented in Ref. [17] were therefore adopted to prevent the building up of trapped modes as was the case in the previous design. The ESRF design is shown at the top of Fig. 2.

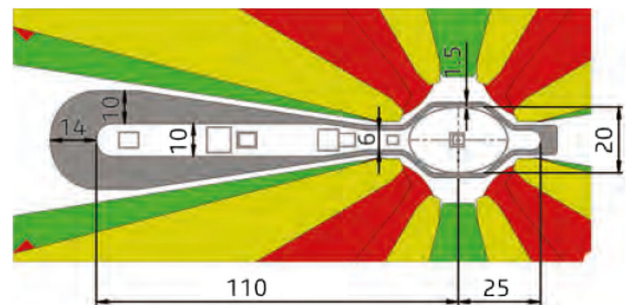


FIG. 1. The vacuum chamber profile for large vertical aperture. The beam passes through the chamber on the right-hand side, while the antechamber on the left is for the synchrotron radiation.

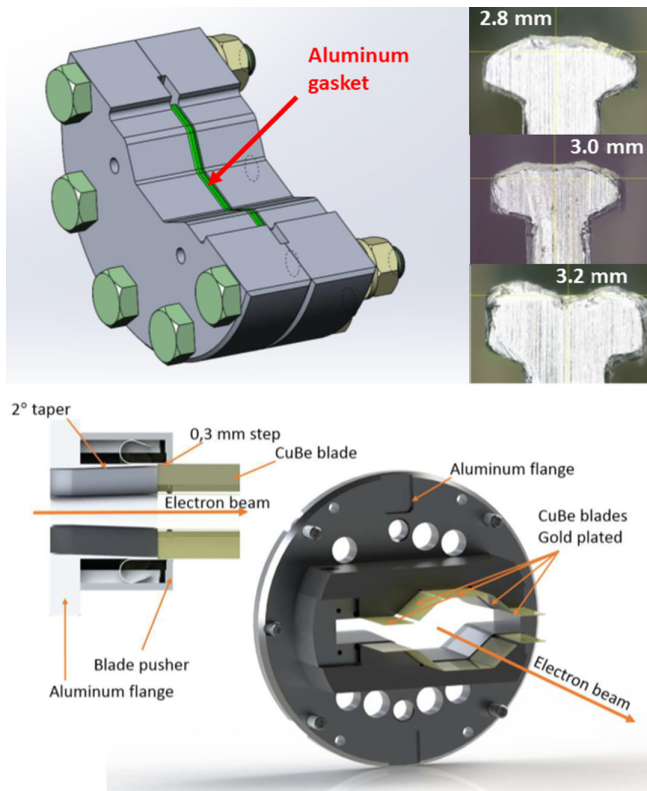


FIG. 2. Low impedance flange (top) and rf fingers (bottom) designs used at ESRF. The top right shows the optimization of the flatness of the gasket.

The aluminum gasket shape was optimized to provide the best flatness while maintaining the electrical continuity between the two flanges. The final design consists of a tee shape plate of 3-mm thickness. rf fingers required both impedance and mechanical optimization. The preceding spring fingers design was subject to frequent failures due to partial or complete loss of electrical contact on one or several fingers resulting in significant local heating of the device and eventually damages requiring vacuum intervention. For these reasons, a more robust design based on sliding fingers (or more precisely blades) was used. This necessitated a complete optimization of the transition from the flange to the fingers (step and taper) as well as the transverse dimensions of the blades to properly shield the bellows. Other critical devices such as IVU, collimators, beam position monitors (BPM), or striplines were optimized as well. After optimization of all the main contributions to the overall impedance, analytical calculations, and tracking simulations were used to derive an estimate for the imaginary effective impedance  $Z_{\parallel}/n$  of  $0.35 \Omega$  that is a factor 2 lower than the value of  $0.7 \Omega$  (defined in detail in Sec. IV A) measured in the old ESRF SR using bunch length versus current data [15]. This value was considered sufficiently low to provide large enough margins to operate the ESRF-EBS at the design maximum single bunch current of 10 mA.

Experience from the previous machine showed that transverse coupled bunch instabilities were dominated by resistive wall and could easily be damped with either mild chromaticity or a transverse bunch-by-bunch feedback [18]. Simulations using a preliminary resistive wall model were performed in the early design phase of the machine and confirmed these observations. In the longitudinal plane, the implementation of higher order mode (HOM) damped cavities removed any risk of developing longitudinal coupled bunch instabilities [19]. Under these assumptions, no significant effort was put into producing a precise long-range wakefield model. This was later confirmed in operation as ESRF-EBS has never suffered any impedance-related coupled bunch instabilities nor was it necessary to use the bunch-by-bunch feedback with the operational chromaticities ( $Q'H = 10$ ,  $Q'V = 7$ ). This report will therefore focus on the real potential limitation, single bunch instabilities.

### III. DEVELOPING THE SHORT RANGE WAKEFIELD MODEL

Once the optimization work and iterations with mechanical engineers have converged to a final design, a precise short range wakefield model is needed to compute single bunch instability thresholds and predict the beam parameters evolution as a function of current. The short range wakefield model can be separated into two categories: geometric and resistive wall (RW).

The geometric wakefield arises from any discontinuities that may occur in the vacuum chamber, its computation is usually performed with finite element electromagnetic (EM) simulation codes by sending an excitation pulse into a 3D meshed model of the element and recording the wakefield on the path of a test particle. The excitation pulse length  $\sigma_z$  will determine the frequency reach of the impedance calculation and needs to be much smaller than the real bunch length used in tracking simulations to cover the full bunch spectrum. While CST Particle Studio was used during the optimization process, the short range wakefield model of the EBS ring is computed by running parallelized simulations on the ESRF cluster using GdfidL [20]. A mesh size of at least  $\sigma_z/10$  and in most cases  $\sigma_z/30$  (in all planes) was used to perform convergence tests for these simulations. This is a factor 2 finer than the mesh size recommended in Ref. [12]. The model includes (i) rf fingers (shielded bellows) and flanges for all chamber profiles; (ii) tapers (rf section, straight section, and transition from small to large profile); (iii) collimators and absorbers; (iv) in-vacuum injection septum; (v) sector valves; (vi) rf cavities; (vii) in-vacuum undulators (in the open position); (viii) ceramic chambers with dedicated short bellows; (ix) diagnostic tools [striplines, BPMs, and current transformers (CTs)].

For each of these elements, the longitudinal, transverse dipole, and transverse quadrupole (for positive and negative



offsets in order to compute the average slope) wake potential was calculated. All elements are calculated separately and then lumped together with proper weighting with  $\beta$  functions. Cross talk between elements and high-frequency modes traveling through the vacuum vessels are therefore neglected and may be a source of systematic error in the model. Elements located in the antechamber have a negligible contribution to the model due to their distance from the circulating beam and are not included. Some more details on the individual contributions of each element to the overall geometric wakefield model can be found in the Appendix.

Simulations were made in CST Particle Studio to determine the RW contribution of each vacuum chamber taking into account its full geometry. This was compared with ImpedanceWake2D (IW2D) [21], which uses an elliptical profile that best matches the chamber geometry. IW2D showed a reduced RW impedance contribution by approximately 20%. This reduction arises due to the fact that the real vacuum chamber is flat and angled (as seen by the outline in Fig. 1) which has openings on the horizontal extremes. This is not taken into account by IW2D which solves for a round case and then applies a Yokoya factor. Therefore, for almost all of the vacuum chambers, the RW component was computed in CST Particle Studio. Only two chambers were modeled in IW2D; the kickers titanium coated ceramic chambers (assuming an approximate elliptical profile) because the thin multilayered coatings were difficult to be accurately modeled in CST, and the NEG coated insertion device (ID) chambers. The optics of the standard cell was split into different vacuum chamber sections and the RW contribution could be appropriately weighted by the average  $\beta$  function across that chamber with the correct material conductivity.

The full wake potential model can be found in Fig. 3. The figure shows that the geometric and RW wake potentials in the longitudinal plane are of similar magnitudes. It can also be seen that the horizontal quadrupolar wake has the opposite sign to the horizontal dipolar wake as expected for a flat chamber geometry.

Convergence studies were performed to validate the choice of the pulse length used in the geometric wakefield calculations. For this purpose, three models were generated using 1-, 3-, and 5-mm pulse lengths. These three models were then used in tracking simulation to compute the evolution of bunch length and energy spread as function of the bunch current. 1-mm is the smallest pulse length that allows for affordable computation duration and memory usage on the ESRF cluster. The results of these simulations showed that for 1-mm pulse length, the energy spread and bunch length had converged at currents greater than 1 mA (and therefore longer bunch lengths). For low current, and therefore shorter equilibrium bunch length, small differences persisted between the three cases. This could be due to inaccurate modeling of the high frequency content and can be a strong source of errors when trying

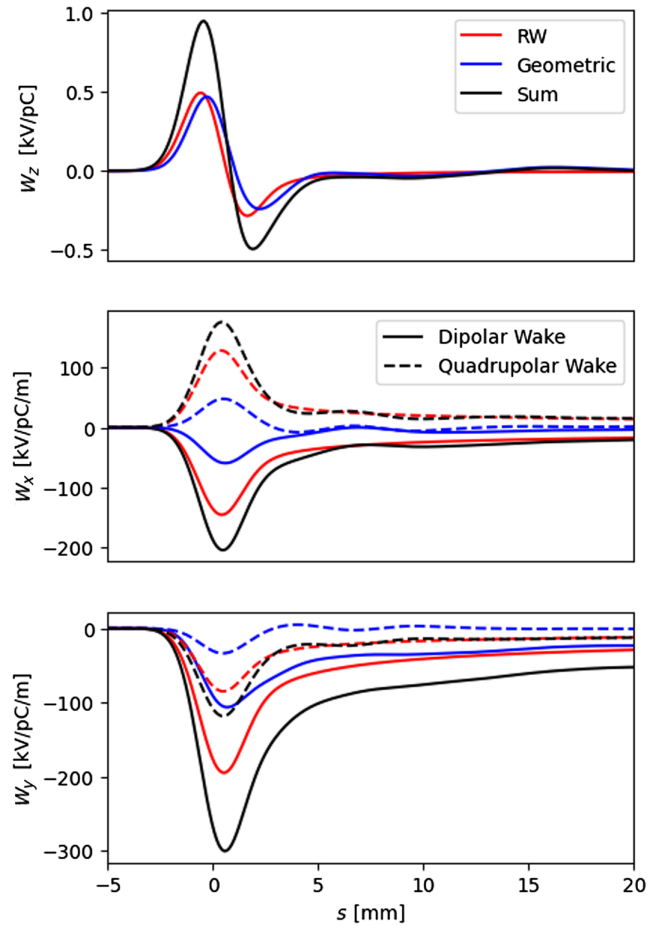


FIG. 3. Longitudinal (top), dipolar (solid), and quadrupolar (dashed) short range horizontal (middle) and vertical (bottom) wake potentials for the EBS for  $\sigma_z = 1$  mm.

to model phenomena that drive high frequency contents in the bunch spectrum such as the coherent synchrotron radiation (CSR) wake or behavior beyond the microwave instability threshold (MWT). Providing the limits in terms of computing capabilities and the good convergence obtained in the determination of global performance parameters, the model with 1-mm pulse length was found to be satisfactory. The reader is referred to Ref. [15] for more information on the convergence studies.

To perform simulations of the single bunch collective effects, PyAT (Python Accelerator Toolbox) was used [22]. The lattice is reduced to a few elements that include a 6D transfer matrix with radiation damping, nonlinear effects (including chromaticity and amplitude detuning), and quantum diffusion to maintain the correct equilibrium emittances in the three planes [23]. This speeds up the computation (as now only three tracking elements are needed compared to approximately 4000 for the full EBS lattice) and can allow a large number of macro particles and slices to be simulated. The lumped wake potential can be included as an element in the lattice, which performs the standard slicing and convolution. For simulations in the longitudinal plane, only the

longitudinal wake potential was included. For the transverse plane, the longitudinal, dipolar, and quadrupolar wake potentials were included to ensure any bunch lengthening effects were taken into account. A simple model for a perfect transverse feedback has also been implemented. The damping time of the feedback is defined in the absence of chromaticity, amplitude detuning, and radiation. A measurement of the damping time was made, which was used as input in the simulations. Typically when comparing collective effects simulations to SR measurements, identical parameters were taken (i.e., the same currents) and the postprocessing of both measurements and simulations was the same. In this report, the simulations and measurements are only provided for the case where the IVU gaps are open, which corresponds to a well-known reproducible state. Closing the IVU gaps changes the energy loss per turn and slightly modifies some of the thresholds presented in this paper, however, the minimum gap varies over time and is difficult to track and properly integrate in the model, only the reproducible case will therefore be presented. The impedance of a closed IVU is well known and can be found in Ref. [24]. This will be implemented into the EBS wakefield model at a later date as it will be crucial to understand the machine limits with low IVU gaps.

#### IV. LONGITUDINAL IMPEDANCE MEASUREMENTS

##### A. Characterization techniques

The longitudinal impedance was characterized with three distinct measurements. The MWT, the bunch lengthening and the synchronous phase shift with current. Before these are introduced in more detail, it is useful to define the effective impedance as [11,25]

$$\left(\frac{Z_{\parallel}}{n}\right)_{\text{eff}} = \frac{\int_{-\infty}^{\infty} Z_{\parallel}(\omega) \frac{\omega_0}{\omega} h(\omega) d\omega}{\int_{-\infty}^{\infty} h(\omega) d\omega}, \quad (1)$$

where  $n = \omega/\omega_0$  is the revolution harmonic number,  $\omega_0 = 2\pi f_0$  is the revolution frequency,  $h(\omega) = \tilde{\lambda}(\omega)\tilde{\lambda}^*(\omega)$  is the bunch power spectrum,  $\tilde{\lambda}(\omega)$  is the Fourier transform of the longitudinal charge density  $\lambda(t)$ . Assuming a Gaussian bunch,  $h(\omega) = e^{-\omega^2\sigma_t^2}$ , where  $\sigma_t = \sigma_z/c$  with  $c$  the velocity of light in a vacuum and  $\sigma_z$  is the rms bunch length.

The MWT is often approximated by the Boussard criterion [26] and is measured by observing a sharp increase in the energy spread of the beam as a function of current.

As can be seen in Fig. 4, in the absence of intrabeam scattering (IBS), the particles below the MWT (left) occupy an elliptical volume in phase space, as expected from a linear model for synchrotron motion. When slightly above the MWT (middle), it can be seen that the bunch has lengthened, but also that tails have begun to appear that spiral outward from the core of the bunch. When well

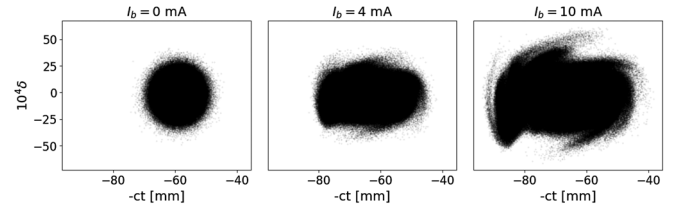


FIG. 4. Simulated longitudinal phase-space plots for three cases. The left shows the zero current, the middle is slightly above the MWT, and the right is well above the MWT.

above the MWT (right), these spirals become much more significant, while the shape of the beam core now deviates from the ellipse. These details imply the presence of high frequencies within the bunch.

In the EBS, there are five pinhole cameras that collect the x rays emitted from either the permanent magnet dipoles or the combined function dipole-quadrupole magnets [27]. The five cameras are situated at one of the two different locations within the standard cell, and each position has different  $\beta$  functions and different dispersions. This means that the energy spread, the horizontal and the vertical emittance can be extracted through a numerical fit. To make a measurement of the MWT, the single bunch current is slowly increased and the energy spread is calculated from the beam spots' sizes.

The second characterization technique that may be used is the bunch length variation with current, which can be approximated with the formula shown in Eq. (2) [28],

$$\left(\frac{\sigma_t}{\sigma_{t0}}\right)^3 - \frac{\sigma_t}{\sigma_{t0}} = \frac{I_b \alpha}{\sqrt{2\pi} \nu_s^2 \omega_0^3 \sigma_{t0}^3 E/e} \text{Im}\left(\frac{Z_{\parallel}}{n}\right)_{\text{eff}} \quad (2)$$

where  $\sigma_{t0}$  is the zero current bunch length,  $I_b$  is the bunch current,  $\alpha$  is the momentum compaction factor,  $\nu_s$  is the synchrotron tune,  $E$  is the beam energy,  $e$  is the elementary charge. The presence of a longitudinal impedance creates an additional longitudinal field which distorts the potential well for the bunch. This can lead to a bunch lengthening (or shortening if the momentum compaction factor is negative).

The last technique used is the bunch phase shift (which is a measure of the energy loss due to impedance) with current. This is directly related to the loss parameter, which is given by [10]

$$k(\sigma_t) = \frac{\omega_0}{\pi} \sum_{p=0}^{\infty} \text{Re}(Z_{\parallel}(p\omega_0)) \exp[-(p\omega_0\sigma_t)^2]. \quad (3)$$

As the bunch loses energy to the impedance, the total energy loss in one turn increases and the synchronous phase changes according to

$$\phi_s = \pi - \arcsin\left(\frac{U_0 + eI_b k t_0}{eV_{rf}}\right), \quad (4)$$

where  $U_0$  is the energy loss per turn to synchrotron radiation,  $t_0$  is the revolution time, and  $V_{\text{rf}}$  is the rf voltage.

## B. Measurements

### 1. Microwave threshold

A measurement of the MWT was made and can be seen alongside PyAT simulations in Fig. 5. The measured MWT was found to be at a value of 1.257 mA, whereas the simulated MWT threshold was found to be at a value of 3.4 mA. This gives a discrepancy on the order of 2.7 times lower threshold (implying that the machine has a larger impedance than modeled). It is clear that there is a strong source of longitudinal impedance in the machine that is not included in the original wakefield model.

One possible source of high frequency impedance could come from CSR [29]. When synchrotron radiation is emitted in the dipoles, the photons are able to interact with electrons in front or behind the source electron through a variety of different phenomena. Due to the short bunch lengths present in light sources, microbunching may occur. In the case of the EBS, the CSR intensity threshold was computed based on the numerical solution to the linearized Vlasov-Fokker-Planck equation [30,31] assuming parallel plate shielding. The computed threshold was only slightly above the maximum single bunch current. This motivated more detailed studies into the impact of CSR. The CSR wake was computed using CSRZ [32], which computes the transient effects at the entrance and exit of the short magnets while considering the impact of the shielding (both parallel plates and with vertical and horizontal shielding). Simulations that include a free space CSR longitudinal wake potential had a large impact on the

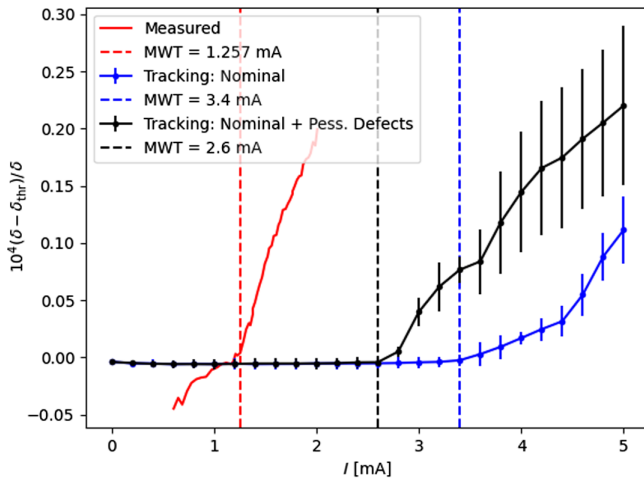


FIG. 5. Measurements and simulations showing the microwave instability, where the dashed line indicates the threshold in each case. The red is data that were measured on the SR, the blue is PyAT tracking with the nominal wake potential, and the black is from PyAT tracking with the wake potential model that includes pessimistic welding defects.

MWT, however, in the EBS, the vertical and horizontal apertures are small so significant shielding of the CSR impedance is observed. This shielding reduces the strength of the longitudinal CSR wake and makes its impact on the MWT negligible.

Another possible source of high frequency impedance could come from welding defects. When two chamber profiles are welded together, the resulting surface is not smooth and small blocks (rectangular or rounded) can occur, as seen in a sketch shown in Fig. 6. These occur in a variety of different places throughout the ring: when a long chamber has been welded together in sections, at the transitions of all the different types of chambers, 1 at each bellow, and 2 at each BPM block. The total number of these defects is estimated to be approximately 2000 and is spread over the large and small aperture chamber profiles. A typical defect can have a maximum height ( $h_d$ ) of 300  $\mu\text{m}$  or a maximum length ( $L_d$ ) of 2.5 mm. Figure 7 shows the impedance of the maximum rectangular defect for large and small vacuum profiles. For the small aperture, resonant peaks are seen at 15 and 38 GHz, whereas for the large aperture, the peaks are seen at 10, 24, and 38 GHz.

To model a pessimistic case of welding defects, defects of maximum possible amplitude were considered. About 80% of these defects were for large aperture vacuum chambers, with 20% for small aperture vacuum chambers. The MWT was simulated and found to be reduced from

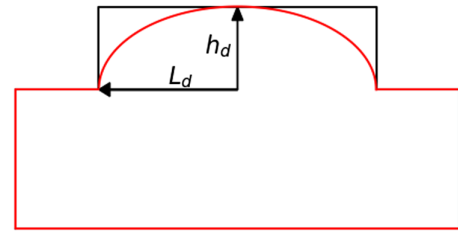


FIG. 6. Sketch showing the geometry of small welding defects on the surface of the vacuum chambers. The black line shows a pessimistic geometry to be modeled, whereas the rounded shape is more realistic.

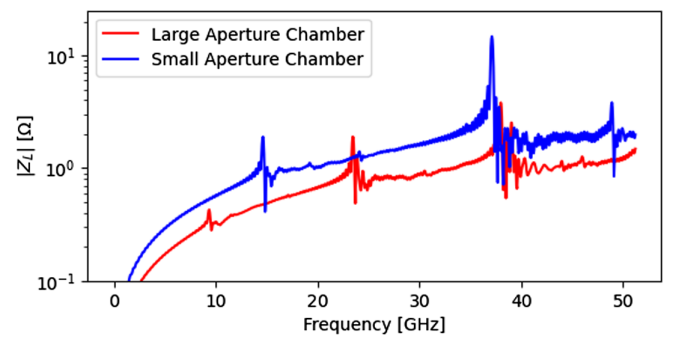


FIG. 7. Longitudinal impedance from a  $\sigma_z = 2$  mm Gaussian beam and a block defect of  $h_d = 0.3$  mm and  $L_d = 2.5$  mm for small and large aperture vacuum chambers.

3.4 to 2.6 mA. Clearly, a step in the right direction but not enough to fully account for the difference in the MWT.

As mentioned earlier, cross talks between adjacent elements are neglected from the model due to each element being simulated independently. The EBS is a very dense machine, with many transitions and sources of geometric impedance occurring close together. It is not certain that this condition is accurate for the EBS, and high frequency impedance sources could arise from coupling between modes in adjacent elements.

Another source of discrepancy can come from the ceramic kickers, which have been heating excessively and currently limit the maximum achievable single bunch current. The titanium coating is vaporized at the transitions into the chamber, which breaks the electrical continuity. This results in additional heating of the kicker chamber, which then cracks due to a weakness in the mechanical design. The flaw in the coating of these kickers is not modeled and could introduce another source of high frequency impedance. These kicker chambers are being replaced with a new design and the MWT will be remeasured after the new kickers' installation. However, the contribution of the kicker impedance to the total machine impedance is small, so it is not expected that this is the sole source of the error.

Finally, as described in Fig. 4, the bunch spectrum in the vicinity of the MWT contains high frequency components which may not be adequately resolved by the wakefield model computed with a  $\sigma_z = 1$ -mm pulse width. This may explain some of the discrepancies seen, as this model with limited frequency resolution could be less efficient in driving the microwave instability.

## 2. Bunch distributions

The bunch profiles and the bunch phase shift can be measured with a dual time base streak camera (Hamamatsu C10910 [33]) installed in the visible light diagnostics beamline of the ESRF. Visible light monitors have been used extensively in third generation synchrotrons, including the ESRF, for many years [34,35]. The visible light contains radiation contributions from the nominal field strength ( $\approx 0.6$  T) of its source magnet and their fringe fields. The light is extracted from the storage ring via a cooled aluminum half mirror, through a UV ultrahigh vacuum window, and steered into a dedicated hutch in the experimental hall.

Measurements of the bunch distribution were made for low single bunch current. The machine was filled to 5 mA in uniform filling, which gives a current of approximately 5  $\mu$ A per bunch. This almost zero current bunch length was measured using the streak camera and was found to be 8% higher than expected. It is believed that this error comes from a systematic error within the streak camera. A series of measurements have been performed on this topic but they are so far inconclusive. There is a strong dependence

of measured bunch length with the sweep speed of the streak camera, with faster speeds showing shorter bunch lengths (the fastest possible measurement giving a bunch length of 3.3 mm) and slower sweep speeds giving larger bunch lengths (the slowest measurement giving a bunch length of 5.4 mm). An investigation into space charge effects within the camera was also performed. A set of neutral density filters was applied to the incoming light to vary the number of electrons created for each bin, however, no impact on the bunch length was observed. Other possibilities are currently being explored. Overestimations of the zero current bunch length with streak camera measurements have also been observed at other facilities [36,37].

The results of bunch distribution measurements with a single bunch as a function of current will now be presented. First, the main features of the distribution, the full width half maximum (FWHM) and the synchronous phase shift will be shown, before looking into more detail at the distributions.

The upper plot of Fig. 8 shows the comparison of the bunch length between measurement and simulation. The FWHM is converted to  $\sigma$  for a Gaussian distribution by dividing by 2.355. The  $\text{Im}(Z_{\parallel}/n)$  was also fitted to the measurement and simulation data using Eq. (2). For low currents, this fitting method works well, but as the bunch becomes more asymmetric, Eq. (2) starts to become less accurate as it is assuming a symmetric Gaussian beam. Nonetheless, comparisons can be made. As can be seen, the results from the simulations show approximately 8%

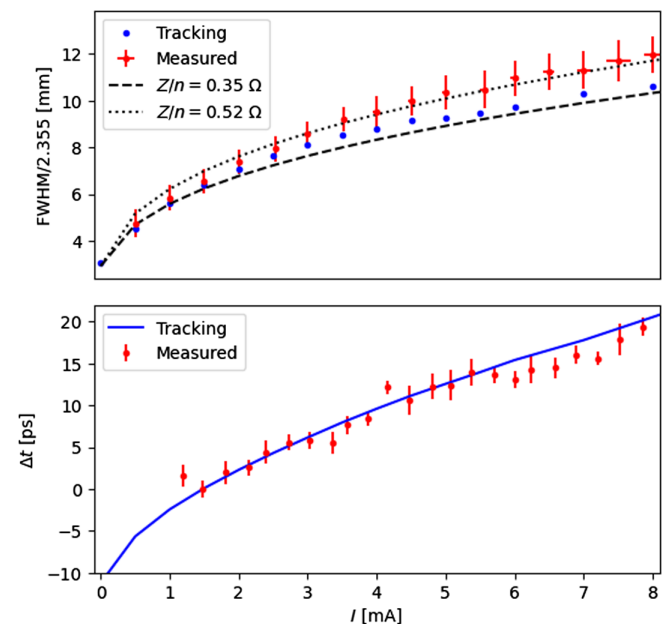


FIG. 8. Top: the measured bunch length versus single bunch current compared with simulations. The dashed lines are solutions of Eq. (2) where  $\text{Im}(Z_{\parallel}/n)$  was fit to the data. Bottom: bunch phase shift versus single bunch current compared to simulation.



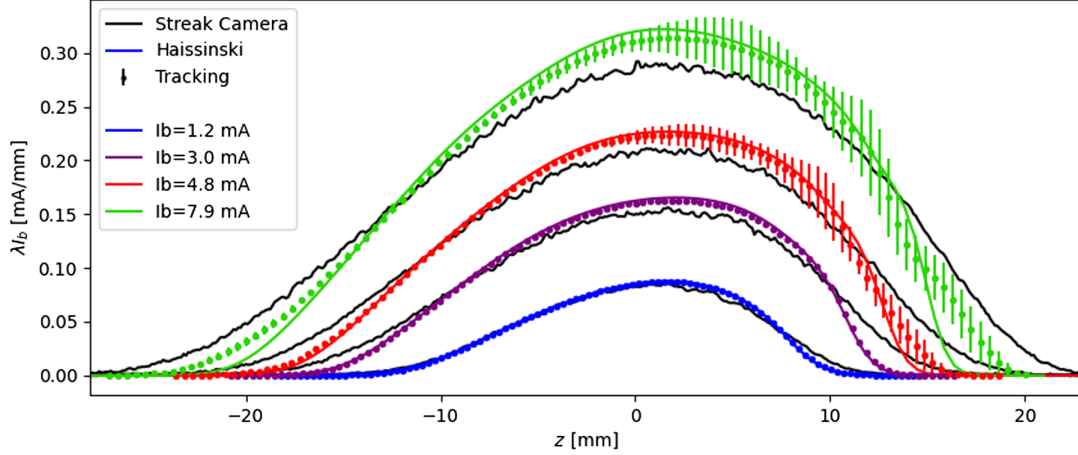


FIG. 9. A comparison between measured bunch distributions (black lines), solutions to the Haissinski equation based on the simulated short range wake model (colored lines), and tracking simulations using the same wake model (points).

shorter bunch length than measured for a current of 8 mA. This corresponds to a  $\text{Im}(Z_{\parallel}/n)$  of  $0.35 \Omega$  for the simulated model versus  $0.52 \Omega$  for the measured data. For the case with defects included (not shown), the simulated bunch length is approximately 5% larger than measured at a current of 5 mA. Given the error on the streak camera measurements at zero current, this bunch lengthening measurement is likely closer than shown here. This would fall well within what is achieved in most other light sources [25].

The lower plot of Fig. 8 shows the bunch phase shift. In this case, the simulation agrees very well with the measurement. The streak camera suffered from jitter on the beam position which was able to be corrected by slicing the full integration range and computing the variation on the center of mass. The error bars reflect the standard deviation of the jitter over the full range.

Drawing a conclusion on the bunch lengthening measurement is difficult due to the large instrumental error on the streak camera. This error puts a strong uncertainty on the tails of the distribution, which has a large impact on the bunch length but has less of an impact on the bunch center of mass. This could explain why the synchronous phase shift measurements agree well but the bunch length measurement is sensitive to the instrumental error despite both measurements coming from the same instrument and the beam sampling the same frequencies of the real and imaginary impedance.

Figure 9 shows a comparison between the electron distributions within the bunch for a selection of beam currents. The figure compares the streak camera measurements (solid black), the distribution from tracking simulations (colored points), and the solution to the Haissinski equation based on the short range wakefield model (solid colors). The Haissinski formula does not include any dynamic effects (for example, the microwave instability), it only solves the equilibrium distribution based on the

potential well distortion [38]. Therefore, below the simulated MWT, it is expected that the simulation will give good agreement with the Haissinski, but above the MWT, some deviation may occur. The multiparticle tracking simulations include the microwave instability, which can affect the distribution of the tails. Therefore, an average of over ten synchrotron periods is taken for each bin. The error bars seen in the figure reflect the standard deviation of these turns. All of the distributions (measured, simulated, and semianalytical) are normalized such that  $\int_{-\infty}^{\infty} \lambda(z) dz = I_b$  and their charge centers are moved to 0. It can be seen from the figure, that when all cases are below the MWT, the agreement is quite good. However, the difference in MWT also affects the agreement of the intermediate cases, as the tail population becomes larger for the measured (above the MWT) than for the simulated (below the threshold for  $I_b = 3.0$  mA and above the threshold for  $I_b = 4.8$  mA).

During the bunch length measurements, the vertical emittance was kept at  $e_v = 10$  pm using the white noise blowup. In a different set of bunch length measurements, the vertical emittance was varied for each current step in order to make a measurement of the contribution of intrabeam scattering (IBS) to the bunch lengthening [39]. The measurements did not show any bunch lengthening at all, even for high single bunch currents with small vertical emittance. Simulations made using ELEGANT [40] showed that for a vertical emittance of 10 pm, up to 3% bunch lengthening could be expected from IBS (peaking at a current of 1.5 mA). This was not observed in the real machine and is still under investigation.

## V. TRANSVERSE IMPEDANCE MEASUREMENTS

A fundamental measurement of the transverse wakefield model is a comparison of the threshold of the transverse mode coupling instability (TMCI) [41]. The bunch oscillation contains different modes at the synchrotron



sidebands, which interact with the impedance spectrum at different frequencies. As the current in the bunch increases, these modes will undergo tune shifts at different rates. At the moment when two modes cross, they begin resonantly exciting one another which causes an instability to develop, characterized by a rapid increase in the oscillation amplitude and typically results in beam loss. For the EBS, the vertical plane is more critical than the horizontal plane due to the smaller vertical aperture, which means that the TMCI occurs first in the vertical plane.

The measurement of the tune shift with intensity up to the TMCI threshold can be seen in Fig. 10. For the measurement, the chromaticity was set to 0 (to within 0.1 units) and the current in the single bunch was increased until an instability developed. The TMCI occurred at  $I_b = 0.44$  mA. The bunch spectrum was also continuously measured by exciting the beam with white noise, as the threshold was approached, this excitation was reduced significantly (which can be seen in the figure) as the beam response began to increase. During this measurement, the vertical and horizontal spectra were obtained and the tune shifts with current were acquired. Table II shows a summary of the predicted and the measured threshold for the TMCI and the tune shift below this threshold. The frequency spectra that were measured were not sharp peaks, but instead noisy plateaus that occasionally contained peaks that moved erratically during the current increase. It was not possible to accurately assign a tune value to this spectrum. To try to account for this, the FWHM of the spectrum was taken and the tune was assigned to be the center of the plateau with the width of the plateau giving the error bar. The size of this plateau (shown by the

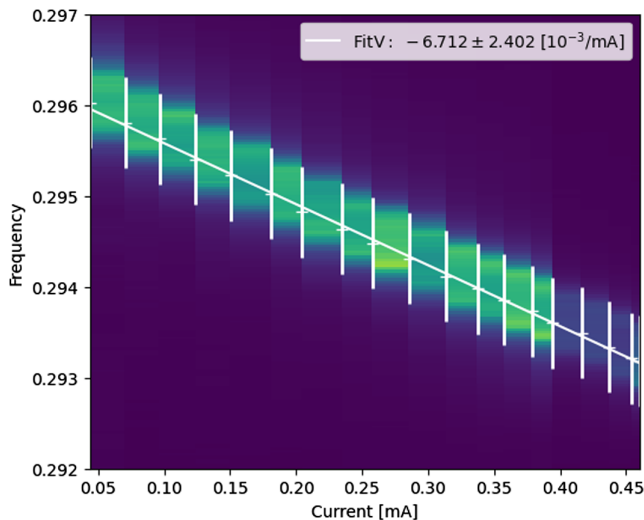


FIG. 10. Vertical tune shift up to the TMCI threshold with a single high current bunch. The large error bars are assigned due to a plateau in the measured bunch spectrum. The TMCI occurred at  $I_b = 0.44$  mA.

TABLE II. Measured mode 0 tune shifts and TMCI thresholds for  $Q'H = Q'V = 0$ , the error on the tune shifts is estimated from the width of the spectrum, which was deformed during the measurements.

	Simulated	Measured	Units
TMCI	0.53	0.44	mA
Tune shift V	-4.988	$-6.712 \pm 2.402$	$10^{-3}/\text{mA}$
Tune shift H	-0.501	$-1.082 \pm 2.228$	$10^{-3}/\text{mA}$

error bars in Fig. 10) is believed to come from quadrupole vibrations.

The final result was computed by taking the shift with current of the center of the plateaus as the main result, and the error on the shift was computed as the difference between the steepest and shallowest gradients. This allows a smooth computation of the average tune shift to be extracted, at the expense of a large error in the measurement.

The measured TMCI threshold is about 20% lower than predicted, indicating the transverse wakefield model is underestimated. As discussed earlier, the dipole and quadrupole wake potentials have opposite signs in the horizontal plane, which are largely canceling each other out. This explains why the tune shift is significantly smaller. In the vertical plane, the wakes have the same sign, increasing the measured tune shift. This is the general case for flat chambers [21]. Both measured tune shifts are larger than predicted.

In order to verify that the mode shift of the first set of synchrotron sidebands behaved as expected, the chromaticity was slightly increased to  $Q'H = Q'V = 1.5$  so that the mode  $-1, 0$ , and  $1$  were all visible in the spectrum. The current was increased and the peaks of each mode were tracked and compared with tracking simulations. This can be seen in Figs. 11 and 12 for the horizontal and vertical planes, respectively. In the horizontal plane, the mode 0 and mode 1 remain relatively flat, while the mode  $-1$  (lower

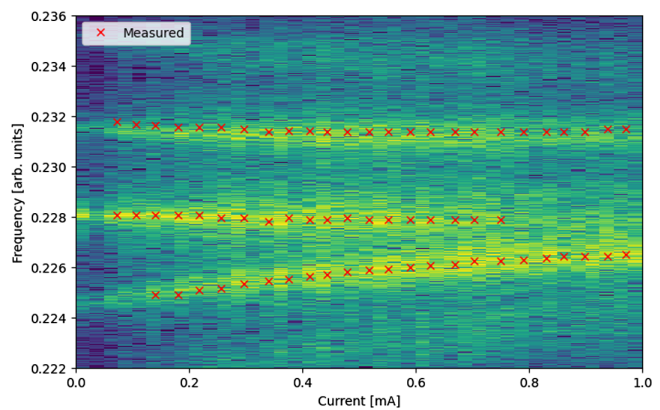


FIG. 11. Horizontal mode shift at  $Q' = 1.5$ . The red crosses are peaks coming from the measured spectrum, whereas the colored background is the simulated spectrum.

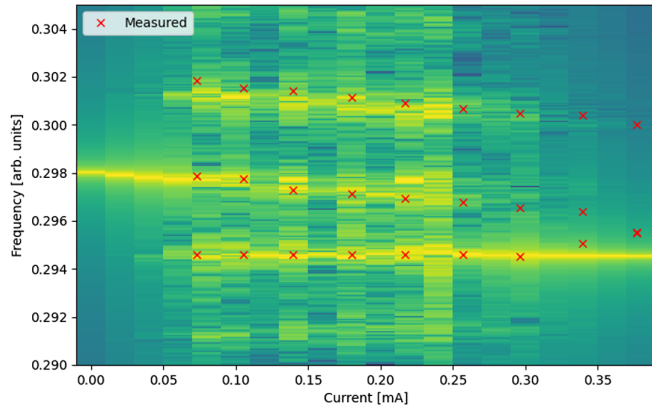


FIG. 12. Vertical mode shift at  $Q' = 1.5$ . The red crosses are peaks coming from the measured spectrum, whereas the colored background is the simulated spectrum.

frequency) increases with current. In the vertical plane, the mode  $-1$  remains flat while the mode  $0$  reduces with current until they couple. The measurements in the vertical plane start to deviate as the modes get closer together and the individual peaks could not be individually resolved due to the limited bandwidth of the measured spectrum. In both cases, the measurements can be well reproduced in the simulations, which highlights that the wakefield model captures all of the key features needed to reproduce the beam behavior.

The head-tail instability threshold as a function of chromaticity has also been measured and compared with simulations for the horizontal and vertical plane. During the measurements, the chromaticity was moved along the diagonal ( $Q'H = Q'V$ ), and for each step, the current was increased until the beam became unstable. Instability in this case is defined, for both measurements and simulations, as exponential increase of the beam centroid position. This initial instability is always in the vertical plane. After this, the vertical transverse feedback was switched on to stabilize the beam and the current could be increased further to allow a measurement of the horizontal threshold. The results of the first scan of the vertical threshold are shown in Fig. 13. The results of the second scan of the horizontal threshold in the presence of a vertical feedback can be found in Fig. 14.

In general, good agreement for the studied chromaticity range is seen when comparing the measured and the simulated thresholds. The maximum single bunch current foreseen in user operation is 10 mA, and it can be seen from the simulation that a chromaticity of 6 is sufficient to stabilize the vertical plane. In reality, this needs to be increased to keep the beam stable during operation ( $Q'H = 10$ ,  $Q'V = 6$ ), especially in the horizontal plane where instabilities may be initiated during the injection process. Additionally, when multiple bunches are present, there is an additional long range RW component that is not considered here. For chromaticities above 6, we were not able to reach the threshold when making the measurement,

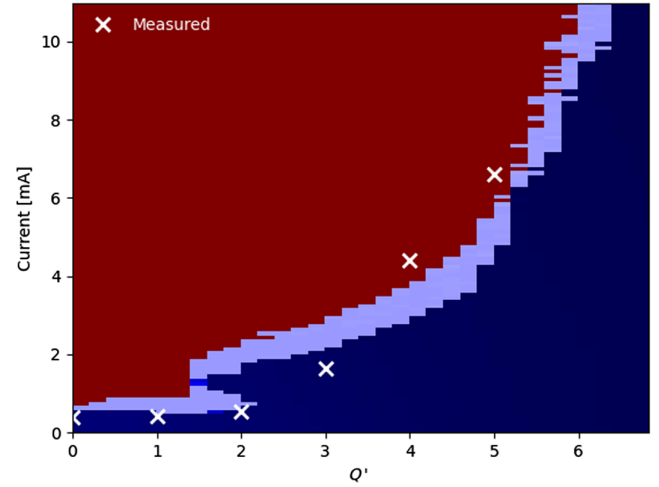


FIG. 13. Vertical instability threshold as a function of chromaticity. The white crosses are measurements and the shaded regions show the simulated area of stability (dark blue) or instability (red, light blue).

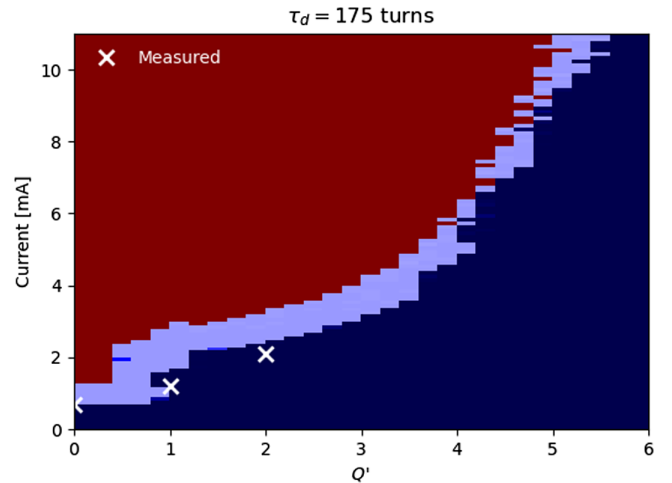


FIG. 14. Instability threshold in the presence of a vertical transverse feedback as a function of chromaticity. The white crosses are measurements of horizontal instabilities and the shaded regions show the simulated area of stability (dark blue) or instability (red, light blue).

as there are limitations due to the heating of the ceramic kickers at high single bunch current. At  $Q'$  between 1 and 2, it is possible to see mode decoupling [42], creating a stable “horn-shaped” region. Further measurements are planned to see if this can be reproduced.

For the horizontal plane, the measured thresholds agree well. It was not possible to make further measurements above  $Q' = 2$  because vertical instabilities began to occur as a result of the saturation of the vertical feedback. Therefore, further measurements were not performed as they would have been too difficult to accurately reproduce in simulation.

## VI. CONCLUSIONS

The wakefield model for the ESRF EBS has been developed and the results of beam based measurements and simulations were compared. The longitudinal bunch lengthening agrees within 8%, but further studies are needed to better understand the systematic errors within the streak camera, whose errors are of a similar magnitude. The bunch phase shift with current also agrees with prediction, highlighting the good characterization of the real effective longitudinal impedance. The MWT has been measured at 1.257 mA, whereas the expected MWT is 3.4 mA in the nominal case or 2.6 mA when considering pessimistic welding defects. This discrepancy has not yet been resolved but can be partially explained by either welding defects or the poor resolution of the wakefield model at high frequencies. CSR and IBS cannot explain this discrepancy. A second iteration on the model, which will include simulation results of more accurate models for some machine elements as well as a detailed defect model, will hopefully reduce the simulated MWT to bring it closer to reality. GdfidL simulation studies for certain machine elements with bunch lengths less than  $\sigma_z = 1$  mm are also planned.

The TMCI threshold was measured to be approximately 20% (0.09 mA) lower than predicted. While the tune shifts at zero chromaticity were generally found to be larger than expected, the error bars on the tune measurement meant a more precise determination of the tune shifts was not possible. Tune shift measurements at low but nonzero chromaticities show that the shifting of the modes can be well reproduced by the simulation. Instability threshold simulations showed that a vertical chromaticity of 6 is enough to stabilize the maximum bunch current of 10 mA. Measurements of this type have shown that 8 mA (the single bunch current limit in the presence of imperfect kickers) was sufficiently stabilized at a vertical chromaticity of 6. For lower chromaticities, good qualitative agreement is seen. A simple vertical transverse feedback model was included in order to explore the horizontal threshold, which showed good agreement for the three measured points, despite being limited in its chromaticity range due to the saturation of the vertical feedback.

Validation of the resistive wall impedance with multi-bunch measurements has already started, with some preliminary intensity threshold and grow damp measurements being taken. Simulations of uniform filling multibunch threshold will be performed in order to compare, while grow damp measurements will be fitted with an analytical formula.

While discrepancies with the MWT have been seen, in general, the longitudinal and transverse wake models provide a useful prediction for machine performance. There are still some additional contributors to the geometric impedance that need to be included which will further increase its accuracy. For example, pumping ports have

been added to the collimators that could couple the beam with a small nearby metal cavity and some special BPMs have been added to the machine that were not yet modeled. All of these inclusions will provide additional impedances that will bring the model closer to reality.

## ACKNOWLEDGMENTS

The authors would like to thank Demin Zhou for fruitful collaboration relating to CSR.

## APPENDIX: BREAKDOWN OF WAKEFIELD MODEL ELEMENTS

In total, 19 components were simulated in GdfidL to model the geometric wakefield. For each element, five simulations were performed, longitudinal, horizontal dipole for positive and negative source offsets and vertical dipole for positive and negative source offsets. The quadrupolar wake could be extracted by computing the wake potential for different test charge offsets for each dipole simulation. For each simulation, a maximum wake distance of 0.1 m was used, this allows a full sampling of the short range wake potential which can be used in a time domain tracking simulation. The loss parameters and kick factors can be computed for each element, which can provide a useful comparison of the relative contributions of each element to the overall wakefield model. This may also allow comparisons with the impedance or wakefield model of other machines. The expression for the computation of the loss parameter is given as [10]

$$k_{\text{loss}} = N_{\text{elem}} \int_{-\infty}^{\infty} d\tau W_z(\tau) \lambda(\tau), \quad (\text{A1})$$

and the expression for the kick factor is given by [10]

$$K_{x,y} = N_{\text{elem}} \langle \beta_{x,y} \rangle \int_{-\infty}^{\infty} d\tau W_{x,y}(\tau) \lambda(\tau), \quad (\text{A2})$$

where  $N_{\text{elem}}$  is the number of occurrences of the element and  $\langle \beta_{x,y} \rangle$  is the average  $\beta$  function at the element. Note that the units of Eq. (A2) are [V/C] due to the multiplication with the average  $\beta$ . When lumping all of the elements together, they are divided by the value of the  $\beta$  function at the observation point.

A summary of all of the detailed wake information can be found in Table III.

To visualize the wake potentials, some grouping needs to be made. The 19 components can be loosely grouped into four categories. These are as follows: (i) Diagnostics (Diag): BPMs, CTs, striplines, collimators, absorbers. (ii) Tapers: cavity tapers, ID tapers, low  $\beta$  tapers. (iii) Shielding: rf fingers, flanges, valves, ceramic chambers. (iv) rf cavity, septum.



TABLE III. Breakdown of simulated machine elements that comprise the geometric short range wakefield model. Large and small refer to the aperture sizes. The  $\beta$  functions are the average  $\beta$  functions at all of the locations of the element. The loss parameter and kick factors include the number of occurrences and  $\beta$  functions.

Element	$N_{\text{elem}}$	$k_{\text{loss}}$ (V/pC)	$\langle\beta_x\rangle$ (m)	$K_x$ (V/pC)	$\langle\beta_y\rangle$ (m)	$K_y$ (V/pC)
Absorber rf	15	13.449	7.36	87.651	3.85	1.139
BPM large	232	13.054	8.42	590.167	6.37	38.308
BPM small	128	17.779	1.52	1559.923	2.88	288.656
CT	2	0.804	6.20	4.505	10.98	29.227
Cavity short damper	13	15.922	7.36	26.856	3.85	0.198
Cavity tapers	3	32.747	7.86	8.277	5.15	825.595
Ceramic chamber	8	1.779	6.75	48.775	10.00	76.014
Collimator	2	2.829	6.20	397.120	10.98	4.416
Fingers large	288	24.725	6.59	804.564	8.15	1137.571
Fingers small	64	8.737	2.02	607.526	2.40	878.014
Flange large	480	16.361	5.77	193.693	9.71	568.498
Flange small	64	3.644	1.82	122.887	2.52	302.187
ID taper	32	70.981	7.86	3301.375	5.15	7507.641
Invac open	12	19.414	7.48	616.572	4.15	1988.036
Low $\beta$ taper	32	2.949	1.85	338.556	2.41	702.588
Septum	1	0.752	18.63	33.490	2.63	3.873
StriplineH	2	0.688	6.20	0.366	10.98	32.896
StriplineV	3	1.481	6.20	84.524	10.98	1.218
Valve	64	5.737	3.61	201.537	12.58	180.875
Total	1445	253.833	...	9028.363	...	14566.951

For each of these groupings, the longitudinal and transverse wake potentials can be plotted. These are shown in Figs. 15–17.

The tapers are the largest contributors to all of the planes of the wakefield model, contributing significantly in the transverse planes and significantly but relatively less in the longitudinal plane. Specifically, the ID tapers are the strongest contributors due to their larger number of occurrences followed by the cavity tapers which are larger individually but occur in fewer places. The low  $\beta$  tapers are relatively weak compared to the other two types of tapers. The tapers are known to have a strong inductive impedance

which contributes strongly to the bunch lengthening. In the EBS lattice, there are many tapers due to the different aperture sections within the standard cell and ID chambers and they are unavoidable. This is why such strict criteria on the taper angle were enforced.

The rf fingers and the flanges are not strong contributors individually, but they have a strong impact across all three planes due to the fact that there are so many of them. The careful design and impedance optimization of the rf fingers and the low impedance flange was critical to maintain an acceptable beam performance.

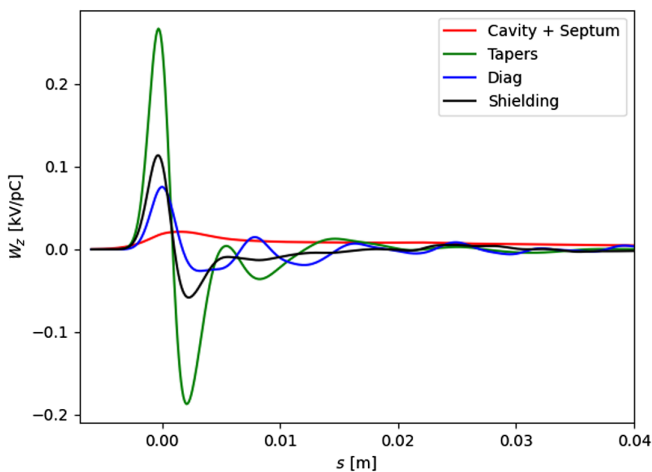


FIG. 15. Longitudinal geometric wake potential.

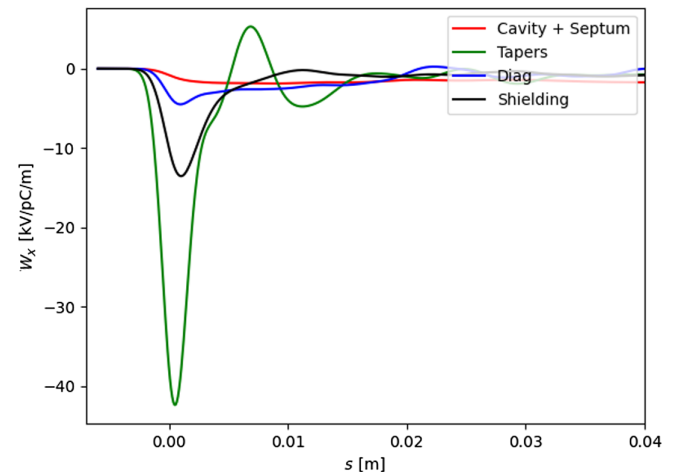


FIG. 16. Horizontal geometric dipolar wake potential.

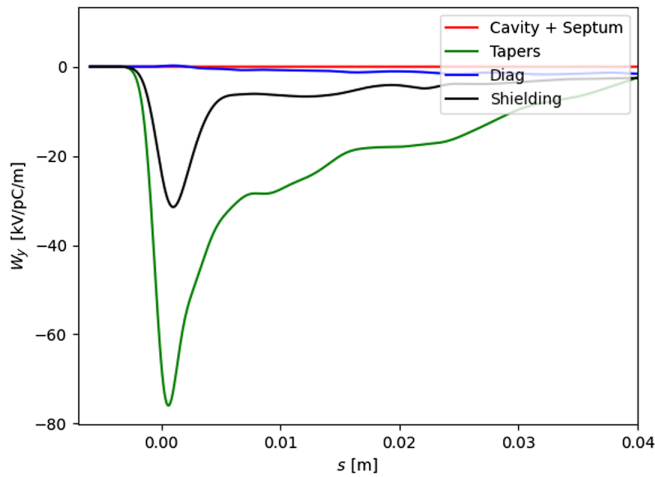


FIG. 17. Vertical geometric dipolar wake potential.

It can be seen that the small aperture BPMs have a strong contribution to the horizontal wake potential. The BPM buttons required impedance optimization due to the fact that they created a narrow band resonator. The radius of the buttons needed to be modified to reduce the shunt impedance of the resonator to below the threshold for coupled bunch instabilities.

- [1] R. Dimper, H. Reichert, P. Raimondi, L. Ortiz, F. Sette, and J. Susini, ESRF Upgrade Programme Phase II (The Orange Book), Technical Design Study Report, ESRF (2014)
- [2] P. Raimondi, N. Carmignani, L. R. Carver, J. Chavanne, L. Farvacque, G. Le Bec, D. Martin, S. M. Liuzzo, T. Perron, and S. White, Commissioning of the hybrid multibend achromat lattice at the European Synchrotron Radiation Facility, *Phys. Rev. Accel. Beams* **24**, 110701 (2021).
- [3] P. Raimondi *et al.*, The extremely brilliant source storage ring of the european synchrotron radiation facility, *Commun. Phys.* **6**, 82 (2023).
- [4] L. Farvacque *et al.*, A low-emittance lattice for the ESRF, in *Proceedings of the 4th International Particle Accelerator Conference, IPAC-2013, Shanghai, China, 2013* (JACoW, Shanghai, China, 2013), pp. 79–81.
- [5] J. L. Revol, J. C. Biasci, N. Carmignani, A. D’Elia, A. Franchi, L. Hardy, I. Leconte, J. Jacob, E. Plouviez, S. M. Liuzzo, H. P. Marques, T. Perron, L. Torino, P. Raimondi, B. Roche, K. Scheidt, and S. M. White, ESRF operation status, in *Proceedings of the 9th International Particle Accelerator Conference, IPAC-2018, Vancouver, BC, Canada* (JACoW, Geneva, Switzerland, 2018), THPMF021, pp. 4088–4091.
- [6] J. L. Revol, R. Nagaoka, P. Kernel, L. Tosi, and E. Karantzoulis, Comparison of transverse single bunch instabilities between the ESRF and ELETTRA, in *Proceedings of the European Particle Accelerator Conference, Vienna, 2000* (EPS, Geneva, 2000), WEP4B06, pp. 1170–1172.
- [7] J. L. Revol, L. Farvacque, L. Hardy, and P. Raimondi, The ESRF from 1988 to 2018, 30 years of innovation and operation, in *Proceedings of the 10th International Particle Accelerator Conference, IPAC-2019, Melbourne, Australia* (JACoW, Geneva, Switzerland, 2019), TUPGW009, pp. 1400–1403.
- [8] SLS 2.0 Storage Ring, Technical Design Report, PSI Bericht, Report No. 21-02, Paul Scherrer Institut, 2021.
- [9] APS-U Storage Ring, Advance photon source upgrade Final Design Report No. APSU-2.01-RPT-003, Argonne National Lab., 2019.
- [10] B. Zotter and S. Kheifets, *Impedances and Wakes in High Energy Accelerators* (World Scientific, Singapore, 1998).
- [11] A. Chao, *Physics of Collective Beam Instabilities in High Energy Accelerators*, 1st ed., Wiley Series in Beam Physics and Accelerator Technology (Wiley, New York, 1993).
- [12] A. Blednykh, G. Bassi, V. Smaluk, and R. Lindberg, Impedance modeling and its application to the analysis of the collective effects, *Phys. Rev. Accel. Beams* **24**, 104801 (2021).
- [13] E. D. Courant, M. S. Livingston, and H. S. Snyder, The strong-focusing synchrotron—a new high energy accelerator, *Phys. Rev.* **88**, 1190 (1952).
- [14] G. Stupakov and D. Zhou, Transverse wakefields due to asymmetric protrusions into a vacuum chamber, *Nucl. Instrum. Methods Phys. Res., Sect. A* **764**, 378 (2014).
- [15] S. White, Preliminary longitudinal impedance model for the ESRF-EBS, in *Proceedings of 8th International Particle Accelerator Conference, IPAC-2017, Copenhagen, Denmark* (JACoW, Geneva, Switzerland), WEPIK058, pp. 3063–3067, [10.18429/JACoW-IPAC2017-WEPIK058](https://doi.org/10.18429/JACoW-IPAC2017-WEPIK058).
- [16] CST Particle Studio, <http://www.3ds.com>.
- [17] H. Matsumoto *et al.*, Experience with a zero impedance vacuum flange at He super-leak temperatures for the ILC, in *Proceedings of the 10th European Particle Accelerator Conference, Edinburgh, Scotland, 2006* (EPS-AG, Edinburgh, Scotland, 2006), MOPLS085, p. 753
- [18] R. Nagaoka, Study of resistive-wall instabilities with a multi-bunch tracking, in *Proceedings of European Particle Accelerator Conference 2002, EPAC2002, Paris, France* (EPS-IGA, Paris, France, 2002).
- [19] A. D’Elia, J. Jacob, and V. Serriere, ESRF-EBS 352 MHz HOM damped RF cavities, in *Proceedings of the 12th International Particle Accelerator Conference, IPAC-2021, Campinas, SP, Brazil* (JACoW, Geneva, Switzerland, 2021), pp. 1034–1036.
- [20] W. Bruns, <http://www.gdfidl.de>.
- [21] N. Mounet, The LHC transverse coupled bunch instability, EPFL, Lausanne, Switzerland, Ph.D. thesis No. 5305, 2012.
- [22] GitHub: Accelerator Toolbox Homepage <https://github.com/atcollab>.
- [23] B. Nash, N. Carmignani, L. Farvacque, S. M. Liuzzo, T. Perron, P. Raimondi, R. Versteegen, and S. White, New functionality for beam dynamics in Accelerator Toolbox (AT), in *Proceedings of the 6th International Particle Accelerator Conference, IPAC-2015, Richmond, VA* (JACoW, Geneva, Switzerland, 2015), MOPWA014, pp. 113–116.
- [24] V. Smaluk, A. Blednykh, G. Rehm, R. Fielder, and R. Bartolini, Coupling impedance of an in-vacuum undulator: Measurement, simulation and analytical estimation, *Phys. Rev. ST Accel. Beams* **17**, 074402 (2014).

- [25] V. Smaluk, Impedance computations and beam-based measurements: A problem of discrepancy, *Nucl. Instrum. Methods Phys. Res., Sect. A* **888**, 22 (2018).
- [26] D. Boussard, Observation of longitudinal microwave instabilities in the CPS, CERN, Geneva, Report No. CERN-LabII/RF/INT-75-2, 1975.
- [27] F. Ewald, P. Elleaume, L. Farvacque, A. Franchi, D. Robinson, K. Scheidt, A. Snigirev, and I. Snigireva, Vertical emittance measurement at the ESRF, in *Proceedings of the 10th European Workshop on Beam Diagnostics and Instrumentation for Particle Accelerators, DIPAC11, Hamburg, Germany* (JACoW, Geneva, Switzerland, 2011), MOPD61, pp. 188–190.
- [28] B. Zotter, Potential-well bunch lengthening, CERN, Geneva, Switzerland, Report No. CERN SPS/81-14, 1981.
- [29] Y. Cai, Coherent synchrotron radiation by electrons moving on circular orbits, *Phys. Rev. Accel. Beams* **20**, 064402 (2017).
- [30] F. Zimmermann, Estimates of CSR instability thresholds for various storage rings, CERN Internal Report No. CERN-ATS-Note-2010-049 PERF, CLIC-Note-861, 2010.
- [31] K. L. F. Bane, Y. Cai, and G. Stupakov, Comparison of simulation codes for microwave instability in bunched beams, in *Proceedings of International Particle Accelerator Conference, Kyoto, Japan* (ICR, Kyoto, 2010), TUPD078.
- [32] D. Zhou, K. Ohmi, K. Oide, L. Zang, and G. Stupakov, Calculation of coherent synchrotron radiation impedance for a beam moving in a curved trajectory, *Jpn. J. Appl. Phys.* **51**, 016401 (2012).
- [33] Hamamatsu Universal Streak Camera, <https://www.hamamatsu.com/eu/en/product/type/C10910-05/index.html>.
- [34] K. Scheidt, Review of streak cameras for accelerators: Features, applications and results, in *Proceedings of the European Particle Accelerator Conference, Vienna, 2000* (EPS, Geneva, 2000).
- [35] K. Scheidt, Dual streak camera at the ESRF, in *Proceedings of the Fifth European Particle Accelerator Conference, EPAC96, Barcelona, Spain* (IOP, Bristol, United Kingdom, 1996).
- [36] U. Iriso and F. Fernandez, Streak camera measurements at ALBA: Bunch length and energy matching, in *Proceedings of IBIC2012, Tsukuba, Japan* (JACoW, Geneva, Switzerland, 2012), TUPA46.
- [37] M. Ries, Nonlinear momentum compaction and coherent synchrotron radiation at the Metrology Light Source, Humboldt University, Ph.D. thesis, 2014.
- [38] K. Bane and R. Warnock, Numerical solution of the Haïssinski equation for the equilibrium state of a stored electron beam, *Phys. Rev. Accel. Beams* **21**, 124401 (2018).
- [39] N. Carmignani, Touschek lifetime studies and optimization of the ESRF: Present and upgraded lattice, University of Pisa, Ph.D. thesis, 2014.
- [40] M. Borland, Elegant: A flexible SDDS-compliant code for accelerator simulation, Advanced Photon Source LS-287, 2000.
- [41] K. Y. Ng, *Physics of Intensity Dependent Beam Instabilities* (World Scientific, Singapore, 2005).
- [42] B. Salvant, Impedance model of the CERN SPS and aspects of LHC single-bunch stability, EPFL, Ph.D. thesis, 2010.